

R4Dyn: Exploring Radar for Self-Supervised Monocular Depth Estimation of Dynamic Scenes

Stefano Gasperini^{*,o,1,2}
Nassir Navab^{1,3}

Patrick Koch^{*,1,2}
Benjamin Busam¹

Vinzenz Dallabetta²
Federico Tombari^{1,4}

¹ Technical University of Munich

² BMW Group

³ Johns Hopkins University

⁴ Google

Abstract

While self-supervised monocular depth estimation in driving scenarios has achieved comparable performance to supervised approaches, violations of the static world assumption can still lead to erroneous depth predictions of traffic participants, posing a potential safety issue. In this paper, we present R4Dyn, a novel set of techniques to use cost-efficient radar data on top of a self-supervised depth estimation framework. In particular, we show how radar can be used during training as weak supervision signal, as well as an extra input to enhance the estimation robustness at inference time. Since automotive radars are readily available, this allows to collect training data from a variety of existing vehicles. Moreover, by filtering and expanding the signal to make it compatible with learning-based approaches, we address radar inherent issues, such as noise and sparsity. With R4Dyn we are able to overcome a major limitation of self-supervised depth estimation, i.e. the prediction of traffic participants. We substantially improve the estimation on dynamic objects, such as cars by 37% on the challenging nuScenes dataset, hence demonstrating that radar is a valuable additional sensor for monocular depth estimation in autonomous vehicles.

1. Introduction

Depth estimation is a fundamental task for scene understanding in autonomous driving and robotics navigation. While learning-based supervised approaches for monocular depth have achieved strong performance in outdoor scenarios [7, 2], the expensive LiDAR sensors required for supervision are not readily available. Additionally, collecting such ground truth data is challenging, and requires further processing, as the raw LiDAR signal may not be sufficient.

* The authors contributed equally.

o Contact author: Stefano Gasperini (stefano.gasperini@tum.de).

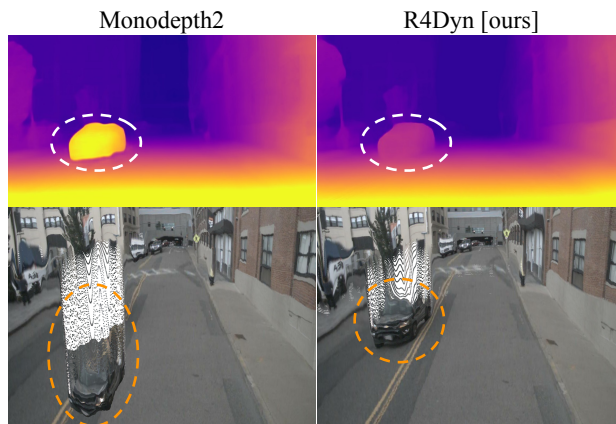


Figure 1. Example of depth prediction of our R4Dyn compared to that of Monodepth2 [11], from the validation set of nuScenes [3]. This dynamic scene violates the static world assumption, posing a challenge for self-supervised approaches. The depth of the safety critical oncoming traffic is severely underestimated by Monodepth2, but correctly predicted by our R4Dyn.

Alternative methods exploit geometrical constraints on stereo pairs or monocular videos to learn depth in a self-supervised fashion. Image sequences offer the most inexpensive source of supervision for this task. However, these approaches require to estimate the camera pose between frames at training time [11], and suffer from inherent issues, such as scale ambiguity and the tendency to incorrectly estimate the depth of dynamic objects.

Furthermore, self-supervised methods rely on the assumption of a moving camera in a static world [30]. As real-world street scenes are typically dynamic, this assumption is often violated, leading to significantly wrong predictions. This raises a variety of issues, such as the infinite depth problem, where leading vehicles driving at the same speed as the camera are predicted to be infinitely far away (such as the horizon), due to their lack of relative motion across frames. Several works addressed this problem either by excluding from the loss computation those regions

where no pixel variation is detected [11], or discarding from the training set those frames with leading vehicles driving at a similar speed [13]. Others increase the complexity by estimating the individual object’s motion [4] or the scene flow [20]. However, existing methods that preserve the model complexity [11, 13] fail to cope with oncoming traffic, as can be seen in Figure 1. In this case, instead of infinitely far, the estimated depth tends to be greatly underestimated, since from the camera perspective its relative motion across frames is larger than that of static objects.

Compared to LiDARs, radars are relatively inexpensive range sensors, already integrated in a large number of mass production vehicles [21, 23], to aid features such as adaptive cruise control. Nevertheless, radar popularity in the learning-based autonomous driving domain is yet limited, and has been explored mainly in the context of object detection [26, 17]. To this date and to the best of our knowledge, only two works [21, 23] investigated the use of radar to improve depth estimation, both proposing a multi-network pipeline to incorporate radar data at inference time, while using LiDAR-supervision during training, transforming the task into sparse depth completion.

In this paper, we aim to bridge this gap and integrate readily available radar sensors to improve self-supervised monocular depth estimation. As radars are already very common, our proposal allows to collect training data from a wide range of existing vehicles, instead of a few prototypes. Despite their inherent noise and sparsity, radars could provide enough information to mitigate the limitations of self-supervised approaches, overcoming the need for LiDARs. Towards this end, we propose a novel loss formulation to complement self-supervised approaches, showing the benefits of radar as additional weak supervision signal to improve on dynamic objects. Moreover, we optionally integrate radar data at inference time, transforming the task into very sparse depth completion. We name our method R4Dyn (Radar for Dynamic scenes), and the contributions of this paper can be summarized as follows:

- We use radar to aid the prediction of dynamic objects in self-supervised monocular depth estimation.
- To the best of our knowledge, this is the first monocular depth estimation work that exploits radar as supervision signal.
- We propose a technique to filter and expand radar detections, and make radar compatible with learning-based solutions.
- We provide extensive evaluations, including errors on safety critical dynamic objects, on the challenging nuScenes dataset [3], training various prior methods under equivalent settings, hence creating a new benchmark, and easing the comparisons for future works.

2. Related Work

2.1. Supervised Monocular Depth Estimation

Estimating depth from a single color image is an ill-posed problem, as there is an infinite number of 3D scenes that can yield the same 2D projection. Nonetheless, tremendous advances have been achieved since Eigen et al. [6] pioneered using CNN-based architectures and Laina et al. [19] leveraged fully-convolutional networks with residual connections [14] to predict dense depth maps from monocular images. While most supervised works regressed directly to the depth measurements of LiDAR sensors (as in KITTI [9]) or RGB-D cameras (as in NYU-Depth v2 [28]), Fu et al. [7] formulated the task in an ordinal fashion.

2.1.1 Depth Completion with Radar

Despite a recently increasing interest in radar for object detection [26, 17], to this date, only two works [21, 23] used it for depth estimation. Both achieved substantial improvements by using it in a LiDAR-supervised setting with a multi-stage architecture, with the first stage filtering the radar signal and improving its quality. In particular, by incorporating the radar as additional input, they transformed the depth estimation task into highly sparse depth completion. Lin et al. [21] were the first to use radar in this supervised context, where they followed a late-fusion approach to account for the heterogeneity of input modalities. Long et al. [23] proposed a sophisticated learning-based association between the projected radar points and the RGB image.

Similarly to these pioneering works [21, 23], our method also incorporates radar for depth estimation, but we follow a novel idea: we focus on using radar to improve the estimation of dynamic objects in a self-supervised setting, for which we propose a specific loss function.

2.2. Self-Supervised Monocular Depth Estimation

Self-supervised methods overcome the need for expensive LiDAR data by leveraging view reconstruction constraints, either via stereo pairs [8, 10] or monocular videos [34, 11, 12]. The latter build on the motion parallax induced by a moving camera in a static world [30]. Furthermore, these methods require to predict simultaneously the depth and the camera pose transformation. Since the pioneering work on video-based training by Zhou et al. [34], vast improvements have been achieved thanks to novel loss terms [11], detail-preserving network architectures [12] and the exploitation of cross-task dependencies [16, 13].

2.2.1 Solutions to Self-supervised Inherent Issues

Scale ambiguity Since infinitely many 3D objects correspond to the same 2D projection, video-based methods

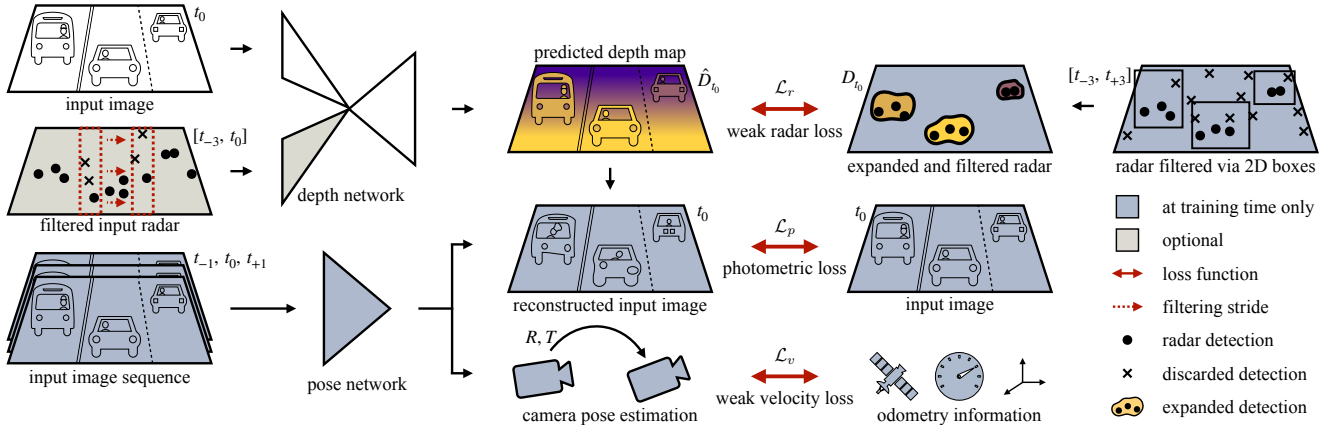


Figure 2. Overview of R4Dyn. The proposed approach incorporates radar as a weak supervision signal, and optionally as additional input. R4Dyn extends a self-supervised framework by incorporating radar to improve on the depth estimation of dynamic objects.

can only predict depth up to an unknown scale factor. Therefore, a plethora of works [34, 11, 4] rely on ground truth (i.e. LiDAR) median-scaling at test time. Guizilini et al. [12] targeted this issue by imposing a weak velocity supervision on the estimated pose transformation, exploiting the available odometry information, achieving scale-awareness.

Dynamic scenes Another major limitation of video-based approaches is due to the inherent static world assumption. This is perpetually violated in driving scenarios, leading to critically incorrect depth predictions of dynamic objects (e.g. traffic participants). A typical failure case is caused by leading vehicles driving at a similar speed as the ego vehicle, thereby lacking relative motion across frames and resulting in a significantly overestimated depth. Godard et al. [11] addressed this problem with an auto-masking loss to ignore pixels without relative motion. In contrast, Guizilini et al. [13] proposed a workaround to detect and discard training samples where this "infinite depth problem" occurs, thereby keeping only uncomplicated frames, albeit reducing the training data.

However, neither of the two [11, 13] accounted for oncoming traffic, which leads to a significantly underestimated depth, since its motion across frames is larger than that of the static elements. This might be linked to the popular KITTI depth benchmark [9] mostly lacking such kind of safety critical dynamic scenes, widely available on nuScenes [3]. Alternative solutions target dynamic scenes, by increasing the model complexity and simultaneously predicting depth, ego-pose, plus 3D motion of dynamic objects [4] or scene flow [33, 24, 15, 20].

Although methods learning scene flow in a self-supervised fashion do not require expensive additional labels, e.g. instance segmentation [4], they might suffer from the same ambiguities of self-supervised depth estimation, and require stereo vision [33, 24, 15].

Our proposed approach is substantially different from previous works targeting dynamic scenes. We address this problem by incorporating radar data, which has not been explored before in this context.

3. Method

In this paper we incorporate radar data to enhance the self-supervised depth prediction of dynamic scenes. An overview of our method can be seen in Figure 2. We build on top of a self-supervised framework which learns from monocular videos, and uses the vehicle odometry (Section 3.1), as in [12], for scale-awareness. Although radar signals are highly sparse and noisy, they could provide enough information to improve self-supervised methods. So, we integrate radar data both during training to improve the prediction of dynamic objects (Section 3.2.3), and inference to increase the overall robustness (Section 3.3).

Radar inherent issues Radar and LiDAR provide significantly different signals: radar signals are noisy, sparse and often lack elevation information. Radar detections projected to the image plane occupy a single pixel, leading to a low density of $\approx 0.03\%$, compared to $\approx 1.63\%$ of a 32-beam LiDAR [3]. Additionally, radar suffers from several sources of noise (clutter), complicating its usage in learning-based approaches. The major causes are multi-path [23] and "see-through" effects, due to the different viewpoints [27], scene geometry and physical sensor properties, and not relatively simple Gaussian noise. Multi-path effects alone affect about 35% of all points [23]. Moreover, due to missing elevation information (e.g. in nuScenes [3]), all detections lie in a plane parallel to the ground. This complicates radar usability, requiring new techniques to make it compatible with learning-based approaches and correctly associate radar detections with image pixels. Therefore, we tackle these issues by expanding the radar influence (Section 3.2.1), and mitigating its noise (Section 3.2.2).

3.1. Self-Supervised Framework

The proposed method is built on top of a video-based monocular depth approach, described in this Section. We aim to simultaneously predict the depth \hat{D}_t of a target frame and the pose transformations $T_{t \rightarrow s}$ between target I_t and source frames $I_s \in \{t-1, t+1\}$. Depth and pose estimates serve to warp the source frames into a reconstructed target view, from which an appearance-based error is computed from the view reconstruction [34] and a Structural Similarity (SSIM) [32] term, as in [11, 12].

Following [11], only the minimum reprojection error \mathcal{L}_p is considered, accounting for partial occlusions. Moreover, pixels without relative motion across frames are masked out [11]. An additional loss \mathcal{L}_s encourages smoothness whilst preserving edges [10]. \mathcal{L}_p and \mathcal{L}_s are computed at each scale of the depth decoder, after upsampling to full resolution [11].

As the radar provides absolute depth values, to use its signal as weak supervision (Section 3.2.3), it is crucial to estimate depth at the right scale. However, as the learning objectives above only allow to predict depth up to an unknown scale factor. We follow [12] to achieve scale-awareness with a weak velocity supervision \mathcal{L}_v on the pose transformation.

3.2. Weak Radar Supervision

In this work, we focus on dynamic objects, which embody safety critical failure cases of self-supervised monocular depth estimation. We aim to mitigate this issue, which is visible in Figure 1, via a weak radar-based supervision.

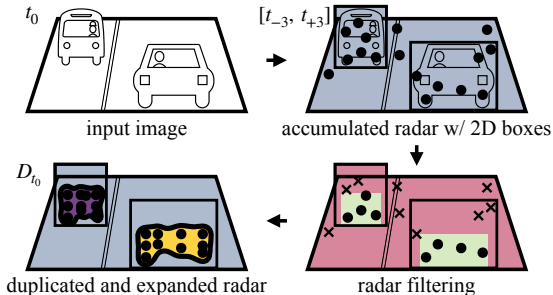


Figure 3. Radar preparation for weak supervision, detail of the top right portion of Figure 2. The signal is accumulated, then filtered via 2D boxes, duplicated and expanded.

3.2.1 Addressing Radar Sparsity

To address radar high sparsity and make it suitable as supervision signal, it is fundamental to expand its influence over a larger portion of the image. In particular, as we focus on dynamic objects, we aim to expand the radar signal across all object pixels, within their boundaries. At training time, we overcome sparsity by incorporating the RGB image context information, similarly to [29, 1], as well as 2D bounding boxes.

Context-aware radar expansion We expand each radar point to cover a larger area of the corresponding object. Expanding it as much as possible, but constraining it within the boundaries, and accounting for 3D shape variations require a precise mapping between the projected radar points and the object pixels. Towards this end, during training, we generate an association map around each radar point. We exploit the idea of bilateral filtering [29], a common edge-preserving image smoothing technique. In particular, we link an image pixel p to a radar point r if p and r are spatially close in the image space, within the same bounding box, and have similar pixel intensities (i.e. $I(p) \approx I(r)$). This bilateral association map can be formalized as follows:

$$w(p, r) = \exp \left(-\frac{(\Delta u)^2 + (\Delta v)^2}{2\sigma_d^2} - \frac{\|\Delta I\|_2^2}{2\sigma_r^2} \right) \quad (1)$$

where $\Delta u = (u - u_r)$ and $\Delta v = (v - v_r)$ are the pixel distances, $\Delta I = I(u, v) - I(u_r, v_r)$ the difference of intensities of a radar point pixel $r = (u_r, v_r)$ and a neighboring pixel $p = (u, v)$, while σ_d and σ_r denote domain and range smoothing parameters, respectively. Hence, the bilateral association $w(p, r)$ represents the probability of a pixel p to be linked to a radar point r .

Pixel-radar association map Although this bilateral confidence map preserves edges by design, it may still leak small, nonzero values beyond object boundaries, leading to undesirably smooth depth predictions. We avoid this by clipping the heatmaps in proximity of the box edges. Moreover, $w(p, r)$ could serve as per-pixel weight for the radar supervision. However, this would put more emphasis on the radar pixel r and result in uneven object depth maps. We address this by transforming the confidence values $w(p, r)$ in a binary map. Considering the set of reliable detections R_{df} (Section 3.2.2) and a threshold $\gamma \in \mathbb{R}$, we compute:

$$W(p, r) = \begin{cases} 1 & \text{if } \max_{r \in R_{df}} w(p, r) > \gamma \\ 0 & \text{otherwise} \end{cases} \quad (2)$$

so all relevant portions get the same amount of supervision.

Duplication To account for the missing elevation, as in Figure 3 we copy each projected radar point r and its corresponding depth along the vertical axis to the lower third and middle of its bounding box. We leave out the upper half of the box to consider depth variations within the boxes (e.g. windshield of the car in the lower part of Figure 4).

Measurement Accumulation We also reduce sparsity by accumulating measurements. To do so, we exploit radar doppler information to compensate for ego- and target-motion across samples, as proposed by [17]. Since the doppler velocity is radial, it provides only a rough estimate of the true velocity of the target, but it is a reasonable approximation considering the frame rate. Via duplication and accumulation, we obtain a dense set of radar points R_d .

3.2.2 Addressing Radar Noise

Noise is another major radar issue to be reduced (Section 3).

Clutter removal We want to extract from R_d reliable measurements R_{df} for supervision. We do so by leveraging 2D bounding boxes during training to filter out noisy radar detections. Within each object in the image space, radar detections closer to the sensor are likely to be reliable, whereas points at higher distances often result from noise. Hence, to obtain R_{df} , we find the minimum depth d_m per bounding box b_i and only keep detections within b_i having $d < d_m + \beta$. The tolerance β allows to keep multiple points in b_i , and accounts for depth variations along 3D objects.

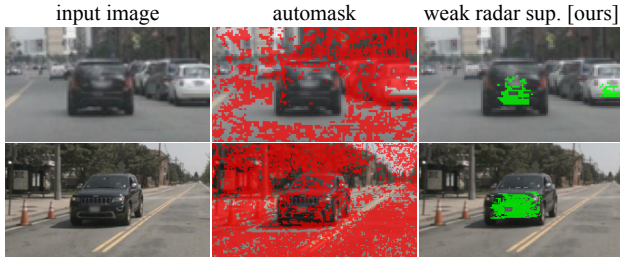


Figure 4. The automask [11] and our radar supervision mask. Red pixels contribute to the loss \mathcal{L}_p . The automask correctly masks out the leading car (top), but not the oncoming one (bottom). Our radar supervision \mathcal{L}_r acts (green) successfully on both cars.

Object-focused filtering Radars without elevation information (e.g. nuScenes [4]) provide only detections parallel to the ground plane, thus, in the image, further points appear higher than closer ones, and within the same objects are more likely to be noisy. Analogously, detections around the box edges could be unreliable due to wide boxes or “see-through” effects. For these reasons, as shown in Figure 3, we discard points in the upper 50% and outer 20% of bounding boxes, as well as overlapping areas. Furthermore, it is more intricate to assess radar detections reliability outside object boxes, hence we discard all background radar points to avoid erroneous supervision.

3.2.3 Training Objective for Dynamic Objects

Addressed noise and sparsity, the radar signal is suitable to weakly supervise the depth prediction of dynamic objects. We want to use it to adjust erroneous depth estimations via a loss function. We define this weak radar supervision as:

$$\mathcal{L}_r(\hat{D}, D) = \frac{1}{N} \sum_{p \in I} \left\| \hat{D}_p - D_p \right\|_1 \odot W(p, r) \quad (3)$$

where \odot denotes the Hadamard product. Eq. 3 aims at fixing the predicted depth \hat{D} towards the expanded target radar measurements D , for each of the N image pixels p where the binary association map $W(p, r)$ (Eq. 2) is positive.

Depth gradient preservation The expanded measurements D in Eq. 3 act as ground truth depth. We introduce $\Omega_j = [W(p, r_j) = 1]$ as the area affected by the expanded radar point $r_j \in R_{df}$. If D was constant within each Ω_j , then \mathcal{L}_r would shift the whole area to the same depth \bar{D} . This would not take into account depth variations within objects, such as the door panels or the windshield of the lower car in Figure 4 being further than its front bumper. Moreover, although the depth of dynamic objects is often under- or over-estimated by video-based self-supervised methods, depth variations within objects are typically well predicted (e.g. in Figure 1). For these reasons, we adapt the pseudo-ground truth D to preserve depth variations. As shown in Figure 5, we do so by computing $\Delta_j = D_{radar}(r_j) - \hat{D}(r_j)$ as the difference between the prediction $\hat{D}(r_j)$ and the measurement $D_{radar}(r_j)$, only at each radar pixel $r_j \in R_{df}$. We then generate the pseudo ground truth $D(\Omega_j)$ by shifting the prediction $\hat{D}(\Omega_j)$ by the same Δ_j :

$$D_j(p) = \hat{D}_j(p) + \Delta_j \quad (4)$$

where Δ_j is computed at the radar pixel r_j such that $\arg \max_{r \in R_{df}} w(p, r_j)$.

The final objective function can thus be formulated as:

$$\mathcal{L} = \mathcal{L}_p + \lambda_1 \mathcal{L}_s + \lambda_2 \mathcal{L}_v + \lambda_3 \mathcal{L}_r \quad (5)$$

with λ_1 , λ_2 and λ_3 being balancing coefficients.

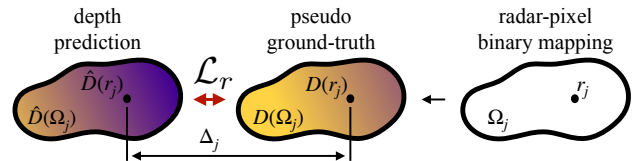


Figure 5. Depth gradient preserving mechanism. We compute Δ_j between prediction and radar detection, then adjust each pixel in the prediction by Δ_j , by enforcing a pseudo-ground truth during training, thereby preserving the predicted gradient.

3.3. Sparse Depth Completion with Radar as Input

As radar sensors are readily available in a wide range of mass-production vehicles [21, 23], a depth estimator could exploit them at inference time, transforming the estimation task in a very sparse depth completion problem. To do so, we first need to mitigate radar inherent sparsity and noise issues. We follow a similar approach as for using the signal as weak supervision (Section 3.2), although we do not make use of 2D bounding boxes at inference time, since extracting them for the input would increase the runtime.

For sparsity, we apply the same measurement accumulation technique described in Section 3.2.1 to obtain a denser point cloud, aggregating the current and past radar frames. For the noise, we adopt the same min-pooling approach as

Method	Sup.	Input	AbsRel	SqRel	RMSE	δ_1	AbsRel _C	AbsRel _V	AbsRel _N	AbsRel _P
Lin et al. [‡] [21]	GT	ImR	0.1086	1.080	5.394	88.21	0.1907	0.2082	0.2088	0.2930
Struct2Depth ^K [4]	Mi*	Im	0.2195	3.799	8.441	73.23	0.3323	0.3516	0.3739	0.2993
PackNet-SfM [12]	Mv	Im	0.1567	2.440	7.230	82.64	0.1814	0.2382	0.2508	0.2473
Monodepth2 [‡] [11]	M*	Im	0.1398	1.911	6.825	84.82	0.1983	0.2110	0.2300	0.2572
baseline [‡] [ours]	Mv	Im	0.1315	1.705	6.520	85.71	0.1862	0.2091	0.2254	0.2351
R4Dyn-L [‡] [ours]	Mvr	Im	0.1296	1.658	6.536	85.76	0.1343	0.1618	0.1686	0.2231
R4Dyn-LI [‡] [ours]	Mvr	ImR	0.1259	1.661	6.434	86.97	0.1250	0.1504	0.1589	0.2146

Table 1. Evaluation on the nuScenes [3] validation *day-clear* set. ‡ were pretrained on ImageNet [5], *K* also on KITTI [9]. Supervisions (Sup.): GT: via LiDAR data, M: via monocular sequences, *: test-time median-scaling via LiDAR, i: instance masks, v: weak velocity, r: weak radar. Inputs (In.): Im: RGB, ImR: RGB and radar. C, V, N and P for *Cars*, *Vehicles*, *Non-parked vehicles* and *Pedestrians*, respectively. R4Dyn-L and R4Dyn-LI: proposed method with radar as L: weak supervision, I: input. Notation reused in other Tables.

in Section 3.2.2, but instead of exploiting 2D boxes, we slide a fixed-size window across all projected radar points.

To account for the fact that radar and camera are heterogeneous sensors, we apply separate encodings and merge the features in a late fusion fashion, as in [21].

4. Experiments and Results

4.1. Experimental Setup

Dataset We conduct all experiments on the challenging nuScenes dataset [3]. We selected it as it is the only available large-scale public dataset with the recording vehicle fitted with a camera and an automotive radar. NuScenes contains around 15h of driving data collected in Boston and Singapore, including diverse traffic scenarios (e.g. both left and right hand drive), with a plethora of dynamic scenes (unlike KITTI [9]), making it difficult for self-supervised depth estimation. As we are interested in sensor setups readily available in production cars, we consider only data from front-facing camera and radar. For training, we use only scenes with good visibility (i.e. *day-clear*). This includes 15129 samples (with synced image, radar and LiDAR data) for the official training set and 6019 for the official validation set (of which 4449 are *day-clear*).

Evaluation metrics We evaluated our models on the standard depth estimation metrics and errors. As ground truth we used single raw LiDAR scans up to a maximum depth of 80m. In particular, as this work focuses on dynamic objects, we are interested in the performance improvements on such objects. Towards this end, we also evaluated according to the semantic class: we exploited LiDAR semantic segmentation annotations from [3] to distinguish between classes, and computed the errors on the depth predictions at the corresponding LiDAR points. The evaluated classes comprise *Cars*, *Vehicles* (e.g. *Cars*, *Trucks*, *Buses*, *Motorcycles*, *Bicycles*), *Non-parked Vehicles* and *Pedestrians*, thereby encompassing all traffic participants.

Network architecture The presented techniques for

processing and incorporating radar data for depth are not tailored to a specific backbone architecture. We used the small and effective ResNet-18-based [14] pose and depth networks from [11]. The pose network comprised 13.0M parameters, while the depth network 14.8M. With the radar as input, an additional ResNet-18 encoder branch was used, increasing the depth parameters by 1.1M.

ID	Weak radar sup.	AbsRel	AbsRel _C
L1	baseline	0.1315	0.1862
L2	L1 + \mathcal{L}_r w/ raw pts	0.1766	0.4841
L3	L2 + filter pts w/ GT box	0.1323	0.1960
L4	L3 + bilateral expansion	0.1306	0.1551
L5	L4 + binary mapping	0.1297	0.1356
L6	L5 + depth gradient pres.	0.1296	0.1343
L7	L6 – GT + predicted box	0.1289	0.1343

Table 2. Weak radar supervision ablation, evaluated on the nuScenes [3] *day-clear* validation set. The baseline L1 is defined in Section 3.1. L3-L6 and L7 make use of 2D boxes from ground truth annotations or an off-the-shelf detector [31], respectively. L6 is equivalent to R4Dyn-L, with image-only input (Im).

Implementation details Each training sample consisted of a 576x320 resolution image triplet (t_{-1}, t_0, t_{+1}) , 4 radar measurements at $[t_{-3}, t_0]$ for the input, and 7 radar samples for the supervision at training time at $[t_{-3}, t_{+3}]$. At inference time we used a single image at t_0 , and 4 radar measurements at $[t_{-3}, t_0]$. Using the Adam optimizer [18] with $\beta_1 = 0.9$, $\beta_2 = 0.999$, we trained with a batch size of 16 for a total of 40 epochs with initial learning rate 2×10^{-4} , which was halved every 10 epochs. If enabled, we introduced the radar supervision after 30 epochs, when the correct depth scale had already been learned, and set the learning rate to 1×10^{-5} , halved after 8 epochs. The loss balancing weights were set to $\lambda_1 = 1 \times 10^{-3}$, $\lambda_2 = 0.02$, $\lambda_3 = 0.2$. During training, we applied random horizontal

flipping to the input data as well color jittering with brightness, contrast, saturation ± 0.2 and hue ± 0.05 to the input images. The window for filtering radar at inference time was 320 pixels tall and 8 wide, with stride 3, while the tolerance β was $2m$. Further details can be found in the supplementary material. In the following, we refer to different configurations of our method, namely R4Dyn-L, R4Dyn-I, and R4Dyn-LI, with -L and -I denoting our weak radar supervision and radar as input, respectively. We trained all models using PyTorch on a single NVIDIA Tesla V100 32GB GPU. Inference of our full method (i.e. R4Dyn-LI) takes 27ms on an NVIDIA GTX 1080 8GB GPU.

ID	Input config.	AbsRel	AbsRel _C
I1	RGB only	0.1315	0.1862
I2	I1 + 1 radar input	0.1357	0.1926
I3	I2 + \mathcal{L}_r	0.1298	0.1319
I4	I3 + radar accum.	0.1301	0.1279
I5	I4 + doppler accum.	0.1273	0.1264
I6	I5 + filtered	0.1259	0.1250

Table 3. Pre-processing ablation for radar as input, evaluated on the *day-clear* nuScenes [3] validation set. I1 is defined in Section 3.1. I6 is equivalent to R4Dyn-LI, our full approach.

Prior works and baseline For a fair comparison, we re-trained all methods on the same dataset split, using the same image resolution, the official implementations and parameters, until convergence. For Struct2Depth [4] we started from model weights pretrained on ImageNet [5] and then KITTI [9] by the authors, which improved its convergence over ImageNet-pretraining only. All methods except for PackNet-SfM [12] used a ResNet-18 [14] backbone pretrained on ImageNet [5]. Our baseline is the self-supervised image-only method described in Section 3.1, which includes the weak velocity supervision.

Radar %	AbsRel	AbsRel _C	AbsRel _V	AbsRel _P
0 %	0.1315	0.1862	0.2091	0.2351
25 %	0.1309	0.1358	0.1672	0.2254
50 %	0.1261	0.1309	0.1553	0.2167
100 %	0.1259	0.1250	0.1504	0.2146

Table 4. Evaluation on the nuScenes [3] *day-clear* validation set. Different amounts of radar points are shown, both for input and weak supervision. 0% is the baseline, while 100% is R4Dyn-LI. C, V and P stand for *Cars*, *Vehicles* and *Pedestrians* respectively.

4.2. Quantitative Results

Comparison with related methods Table 1 shows the comparison between our R4Dyn and related approaches.

We report alternative solutions for dynamic objects, such as Struct2Depth [4] and Monodepth2 [11], as well as another method using radar for depth, i.e. the LiDAR-supervised work by Lin et al. [21]. Our R4Dyn-L and R4Dyn-LI outperformed the strong baseline across the board, by a significant margin. Remarkably, the error on *Cars* dropped by a substantial 33% with R4Dyn-LI, showing the benefit of radar for estimating the depth of dynamic objects. Our approach largely improved over Monodepth2 [11], on which our baseline builds upon. As can also be seen in Figure 4, the automask from Monodepth2 [11] was not able to cope with oncoming traffic, occurring frequently in the nuScenes dataset. This led to a large error on *Cars* and other traffic participants. Our R4Dyn-L and R4Dyn-LI reduced it by 32% and 37% respectively.

Method	<i>all</i>	<i>clear</i>	<i>rain</i>	<i>night</i>
Lin et al. [21]	0.126	0.109	0.145	0.248
Struct2Depth [4]	0.238	0.220	0.271	0.336
PackNet-SfM [12]	0.168	0.157	0.177	0.262
Monodepth2 [11]	0.161	0.140	0.193	0.287
baseline [ours]	0.146	0.132	0.166	0.242
R4Dyn-L [ours]	0.147	0.130	0.164	0.273
R4Dyn-LI [ours]	0.137	0.126	0.146	0.219

Table 5. Evaluation of AbsRel to generalize on adverse and unseen conditions of the validation set of nuScenes [3]. All methods were trained on *day-clear* (*clear*).

Struct2Depth [4], despite being additionally pretrained on KITTI [9] and its individual motion predictions, produced the worst estimations, with large inconsistencies (AbsRel std. 0.1511). Our R4Dyn-LI outputs were far more consistent (std. 0.079). We attribute this difference to the superiority of radar over instance masks as weak supervision, as well as to Struct2Depth [4] not fully solving the infinite depth problem (e.g. in Figure 6). The sophisticated PackNet architecture [12] was not able to deliver satisfactory results, which could be due to the larger model size (129M instead of 15M for ResNet-18), and the relatively small dataset. This motivated using ResNet [14] as backbone. Furthermore, the LiDAR-supervised work by Lin et al. [21], with radar as input, performed better than ours overall, albeit worse on safety critical traffic participants, such as by 53% on *Cars*. This could be due to the sparsity of the LiDAR from which it learned. Overall, Table 1 demonstrates the benefit of radar for monocular depth estimation, as it can substantially improve the predictions of safety critical dynamic objects, both as weak supervision with R4Dyn-L and as input with R4Dyn-LI.

Weak Radar supervision ablation study Table 2 shows the impact of the various components of our weak radar supervision. Throughout the table, errors do not decrease with

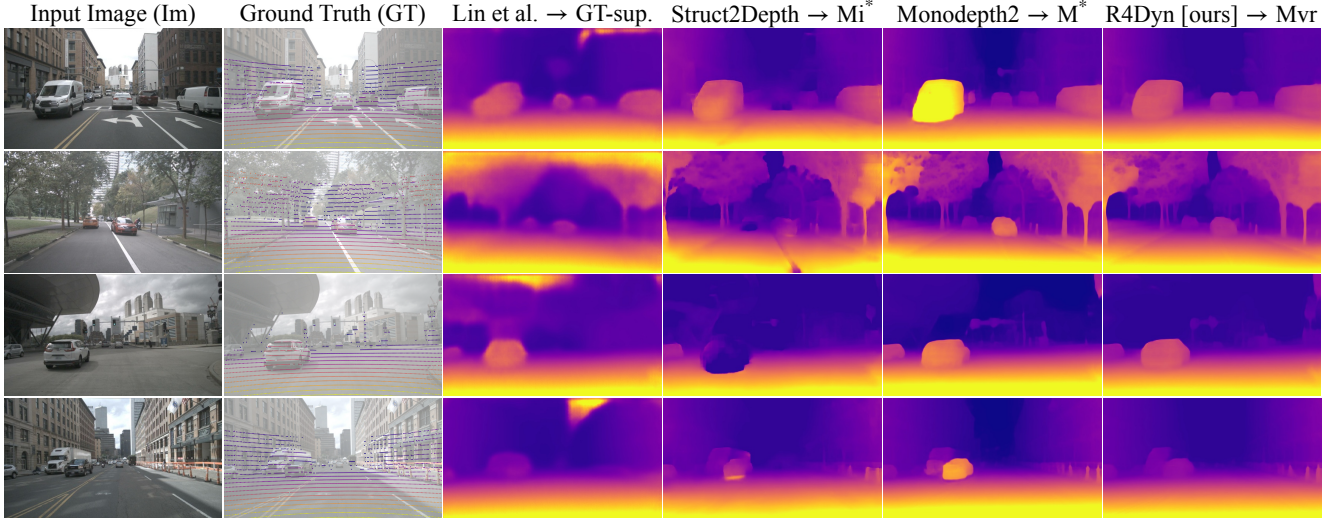


Figure 6. Qualitative results from related works on the nuScenes [3] validation set. Next to each method name we indicate its supervision.

the introduction of each and every feature, thereby confirming that the radar signal necessitates to be filtered (row L3) and expanded (L4) before it can positively contribute over the baseline (L1), while simply integrating the raw points (L2) increased the errors. With L7, we show that 2D bounding boxes can be extracted via an off-the-shelf detector, such as Scaled-YOLOv4 [31] trained on MS COCO [22], removing the need for ground truth annotations. L7 improved over L6 (which used ground truth boxes), presumably due to the nuScenes [3] boxes being oversized (used in L3 to L6). Overall, Table 2 confirms the importance of our modifications to use radar as weak supervision.

Radar as input ablation study Table 3 reports various configurations for using radar as input, again motivating the expansion (I4 and I5) and filtering (I6) of the radar signal. In fact, simply adding a single radar sweep in input (I2) did not outperform the baseline (I1).

Variable amount of radar signal In Table 4 we show how the output quality changed by excluding a variable amount of radar detections from the dataset. Already 25% of the radar detections brought a large improvement over the baseline (0%), overall as well as on safety critical traffic participants. Once again, this shows the benefit of radar for depth estimation, despite its inherent noise and sparsity. In particular, adding more detections (filtered and expanded), systematically reduced all the errors. Moreover, considering the rapid progressing of sensor technology [25], higher resolution (e.g. 200%, 400%) and less noisy automotive radar sensors might be available in the future, which would further increase the gap to the RGB-only baseline.

Generalization to unseen adverse conditions Table 5 reports AbsRel of our R4Dyn and related methods on difficult unseen conditions. This shows the ability of each to generalize to different data distributions. Our R4Dyn-LI

outperformed all self- and weakly-supervised approaches in all conditions. Compared to the LiDAR-supervised work by Lin et al. [21], R4Dyn-LI performs similarly in rain and significantly better in night scenes, reiterating the effectiveness and robustness of our techniques.

4.3. Qualitative Results

Qualitative results in Figure 6 confirm the findings of our experiments, showing the superiority of our R4Dyn in estimating the depth of traffic participants. In particular, Struct2Depth [4] had frequent issues with leading vehicles (first 3 scenes), and added a halo effect to the oncoming car in the fourth scene. Monodepth2 [11] was able to correctly estimate leading vehicles, thanks to its automask, but not oncoming traffic (as seen in Figure 1 and inspected in Figure 4), which resulted in severe underestimations (first, second and fourth scene). The LiDAR-supervised work by Lin et al. [21] correctly estimated the overall depth, but missed most details, delivering blurred outputs. Instead, our R4Dyn could accurately estimate all challenging dynamic scenes, preserving sharp details.

5. Conclusion

In this paper we proposed R4Dyn, a set of techniques to integrate radar into a self-supervised monocular depth estimation framework. Extensive experiments showed the benefit of using radar both during training as weak supervision, and at inference time as added input. Our method substantially improved on the prediction of safety critical traffic participants over all related works. Therefore, R4Dyn constitutes a valuable step towards robust depth estimation. Additionally, the inexpensive and readily available setup required, allows to collect training data from a variety of existing vehicles, removing the need for expensive LiDAR data.

A. Supplementary Material

In this Section we include further details and additional results computed from the same models reported in the main manuscript.

A.1. LiDAR and Radar

In Figure 7 we show the significant difference between LiDAR and radar signals. As described in Section 3, due to the physical properties of the sensor, radar signals are noisy, sparse and often 1-dimensional. The complex multi-path noise can be seen affecting the two points marked by arrows in the Figure. Despite their mutual distance of 5.2 meters, the points are projected onto the same foreground object in the image space. This once again shows the importance of our modifications to handle radar data for weak supervision (Section 3.2.3).



Figure 7. LiDAR (left) and radar (right) signals from nuScenes [3]. The two radar measurements marked by arrows are 5.2 meters apart, due to multi-path effects.

A.2. Self-supervised Framework

In the following, we further specify the loss functions described in Section 3.1. The photometric loss is a combination of \mathcal{L}_1 -loss and SSIM [32], as in [10]:

$$\begin{aligned} \mathcal{L}_1(I_t, \hat{I}_t) &= \|I_t - \hat{I}_t\|_1 \\ \mathcal{L}_{\text{SSIM}} &= 1 - \text{SSIM}(I_t, \hat{I}_t) \\ pe(I_t, \hat{I}_t) &= (1 - \alpha) \mathcal{L}_1(I_t, \hat{I}_t) + \frac{\alpha}{2} \mathcal{L}_{\text{SSIM}}(I_t, \hat{I}_t) \end{aligned} \quad (6)$$

where $\alpha = 0.85$ balances between the \mathcal{L}_1 and the SSIM term. Additionally, as in [11], we only consider the minimum reprojection error to account for partial occlusions:

$$\mathcal{L}_p(I_t, \hat{I}_{s \rightarrow t}) = \min_s pe(I_t, \hat{I}_{s \rightarrow t}). \quad (7)$$

Furthermore, we follow [11] by automatically masking out pixels which do not change appearance in between frames:

$$M_a = \min_s \mathcal{L}_p(I_t, I_s) > \min_s \mathcal{L}_p(I_t, \hat{I}_{s \rightarrow t}). \quad (8)$$

Hence, the photometric loss is only considered in regions where $M_a = 1$. Moreover, to encourage local smoothness

while preserving edges we use a specific term from [10]:

$$\mathcal{L}_s(I_t, d_t^*) = \frac{1}{N} \sum_{p \in N} \sum_{i \in x, y} |\partial_i d_t^*(p)| e^{-|\partial_i I_t|} \quad (9)$$

where $|\cdot|$ denotes the element-wise absolute value, ∂_x and ∂_y are gradients in x- and y-direction, and $d_t^* = d_t^*/\bar{d}_t^*$ the mean-normalized inverse of the depth prediction.

As described in Section 3.1, we follow [12] with a weak velocity supervision \mathcal{L}_v for scale-awareness:

$$\mathcal{L}_v(\hat{\mathbf{t}}_{t \rightarrow s}, \mathbf{t}_{t \rightarrow s}) = \left| \|\hat{\mathbf{t}}_{t \rightarrow s}\|_2 - \|\mathbf{t}_{t \rightarrow s}\|_2 \right| \quad (10)$$

where $\hat{\mathbf{t}}_{t \rightarrow s}$ and $\mathbf{t}_{t \rightarrow s}$ are the predicted and ground truth pose translations respectively, easily obtainable from readily available velocity information (e.g. via odometry).

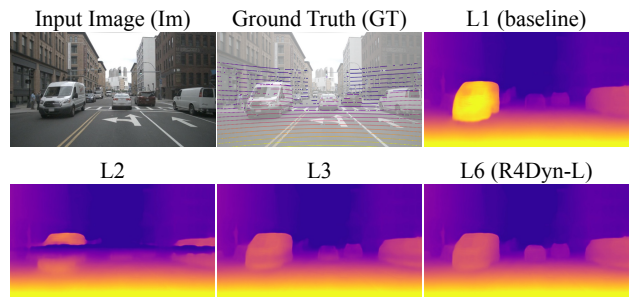


Figure 8. Qualitative comparison complementing the ablation study on the weak radar supervision (Table 2).

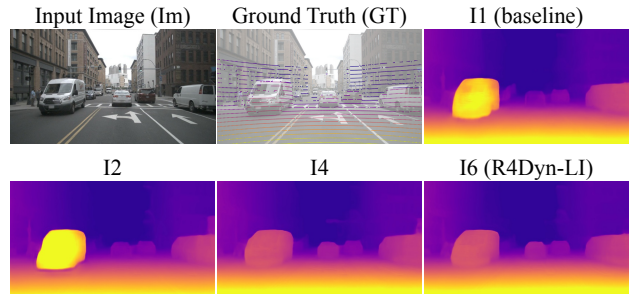


Figure 9. Qualitative comparison complementing the ablation study on the pre-processing for radar as additional input (Table 3).

A.3. Radar Accumulation

The accumulation of multiple radar measurements described in Section 3.2.1 is performed by mapping points from time $t - \tau$ to t , as proposed by [17]. Specifically, the ego- and target-motion compensation across multiple measurements is done considering the doppler velocity as:

$$\begin{aligned} x_t &= x_{t-\tau} + \Delta d_{x,t} + v_{x,t-\tau} \cdot \Delta\tau \\ y_t &= y_{t-\tau} + \Delta d_{y,t} + v_{y,t-\tau} \cdot \Delta\tau \\ z_t &= z_{t-\tau} + \Delta d_{z,t} \end{aligned} \quad (11)$$

where x_t , y_t and z_t denote the estimated target location at time t , Δd the ego pose transformation between measurements, and v the measured doppler velocity of the target.

A.4. Additional Implementation Details

As we focus on safety critical dynamic objects (e.g. traffic participants), when filtering the radar signal to use it as weak supervision (Section 3.2), we only consider 2D bounding boxes of the following classes of nuScenes [3]: *Vehicles* (including all sub-classes) and *Pedestrians* (including all sub-classes). As nuScenes provides only 3D bounding boxes, we obtained 2D boxes by considering the top, left, bottom, and right extremes of the projected 3D boxes. Furthermore, as we want to expand the radar signal over the objects, the binary association mask from Equation 2 should vary in size depending on the object, e.g. larger for a bus, than for a pedestrian. Additionally, we consider as most reliable detections those projected in the lower center of a bounding box. Towards this end, we set the smoothing parameter σ_d according to the bounding box dimensions, hence accounting for the object size: we set

Method	<i>all</i>	<i>clear</i>	<i>rain</i>	<i>night</i>
<i>Cars</i>				
Lin et al. [21]	0.217	0.191	0.225	0.433
Struct2Depth [4]	0.346	0.332	0.320	0.535
PackNet-SfM [12]	0.219	0.181	0.270	0.449
Monodepth2 [11]	0.232	0.199	0.261	0.486
baseline [ours]	0.212	0.186	0.240	0.391
R4Dyn-L [ours]	0.164	0.134	0.219	0.311
R4Dyn-LI [ours]	0.140	0.125	0.171	0.204
<i>Vehicles</i>				
Lin et al. [21]	0.229	0.208	0.233	0.428
Struct2Depth [4]	0.361	0.352	0.335	0.535
PackNet-SfM [12]	0.259	0.238	0.274	0.440
Monodepth2 [11]	0.240	0.211	0.270	0.483
baseline [ours]	0.231	0.209	0.259	0.384
R4Dyn-L [ours]	0.182	0.162	0.220	0.308
R4Dyn-LI [ours]	0.159	0.150	0.176	0.200
<i>Pedestrians</i>				
Lin et al. [21]	0.292	0.293	0.254	0.401
Struct2Depth [4]	0.298	0.299	0.276	0.367
PackNet-SfM [12]	0.252	0.247	0.284	0.355
Monodepth2 [11]	0.258	0.257	0.253	0.317
baseline [ours]	0.238	0.235	0.244	0.348
R4Dyn-L [ours]	0.229	0.223	0.255	0.409
R4Dyn-LI [ours]	0.218	0.215	0.234	0.332

Table 6. Evaluation of AbsRel on *Cars*, *Vehicles* and *Pedestrians* under adverse conditions of the validation set of nuScenes [3]. All methods were trained only on scenes with *day-clear* (*clear*) conditions. This Table complements Table 5, therefore shows the ability of each method to generalize to unseen settings.

$\sigma_{d,x} = c \cdot s \cdot bb_w/2$ and $\sigma_{d,y} = c \cdot s \cdot bb_h/2$, where bb_w and bb_h are the box width and height, and c is a constant scale factor set to 1.5. Moreover, s is a scale factor that depends on the position of the considered radar point with respect to the bounding box: $s = \delta_{side}/(bb_w/2) \cdot \delta_{top}/bb_h$, with δ_{side} and δ_{top} being the minimum distance of the radar point from the bounding box side and top edges respectively. The range smoothing parameter is fixed to $\sigma_r = 1 \times 10^{-5}$.

For prior works, as mentioned in Section 4.1, we used the original implementation and parameters, adapted as follows to accommodate the different dataset (i.e. nuScenes [3]). We trained Monodepth2 [11] for 40 epochs, which is the same as our R4Dyn. PackNet-SfM [12] was trained for a total of 200 epochs due to its slow convergence, and Struct2Depth [4] was trained for 75 epochs after the full KITTI [9] training performed by the authors. For fairness when comparing with other approaches, for Struct2Depth [4] we used the motion model (denoted by the authors with an M), but not their online refinement (indicated with an R). To ensure fair comparability with other methods, for the work of Lin et al. [21] we only used radar measurements from the past and present, but not from the future, which were used in the original implementation.

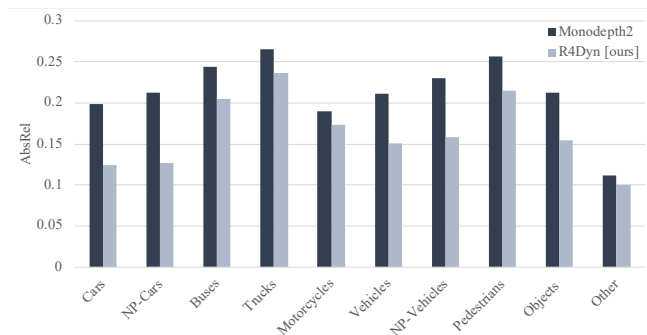


Figure 10. The histogram shows a class-wise evaluation of our R4Dyn and Monodepth2 [11] on the nuScenes *day-clear* validation set [3]. *Other* includes all remaining classes, that are not traffic participants, and *NP* indicates *Non-Parked Cars* or *Vehicles*. Lower absolute relative (AbsRel) error is better.

A.5. Additional Results

A.5.1 Qualitative Ablation Studies

In Figures 8 and 9 we show highlights of the qualitative results of our ablation studies on the weak radar supervision and additional radar input, respectively. These complement the quantitative results reported in Tables 2 and 3 with the sample being the same as the first one in Figure 6 for consistency. In the Figures, it can be seen how our image-only baseline (L1 and I1) performs similarly to Monodepth2 [11] on which it is based. Then, in Figure 8, adding a weak supervision by raw radar points (L2) deteriorated the estimations due to the considerable amount of noise caused by

Cl.	Method	Sup.	Input	AbsRel	SqRel	RMSE	RMSE _{log}	δ_1	δ_2	δ_3
<i>Cars</i>	Lin et al. [21]	GT	ImR	0.1907	2.399	6.922	0.2460	75.71	91.02	96.06
	Struct2Depth [4]	M*	Im	0.3323	7.436	9.353	0.3307	57.38	80.54	89.98
	PackNet-SfM [12]	Mv	Im	0.1814	1.936	6.313	0.2341	72.88	91.02	96.46
	Monodepth2 [11]	M*	Im	0.1983	2.100	6.635	0.2509	68.23	88.76	94.81
	baseline [ours]	Mv	Im	0.1862	2.115	6.735	0.2495	70.41	87.96	94.41
	R4Dyn-L [ours]	Mvr	Im	0.1343	1.481	5.713	0.1913	81.45	94.02	97.32
	R4Dyn-LI [ours]	Mvr	ImR	0.1250	1.371	5.395	0.1813	84.14	94.38	97.43
<i>NP-Cars</i>	Lin et al. [21]	GT	ImR	0.1898	2.485	6.793	0.2418	77.15	90.69	95.65
	Struct2Depth [4]	M*	Im	0.3703	9.063	10.05	0.3472	54.42	78.15	88.35
	PackNet-SfM [12]	Mv	Im	0.1902	2.050	6.397	0.2394	70.56	90.35	96.20
	Monodepth2 [11]	M*	Im	0.2130	2.368	6.905	0.2624	65.05	87.03	93.97
	baseline [ours]	Mv	Im	0.1862	2.115	6.735	0.2495	70.41	87.96	94.41
	R4Dyn-L [ours]	Mvr	Im	0.1356	1.518	5.651	0.1894	80.92	93.56	97.16
	R4Dyn-LI [ours]	Mvr	ImR	0.1274	1.399	5.302	0.1793	83.80	94.01	97.43
<i>Buses</i>	Lin et al. [21]	GT	ImR	0.2330	3.336	8.456	0.2728	65.46	85.48	93.44
	Struct2Depth [4]	M*	Im	0.3962	7.487	12.11	0.4057	41.22	69.19	85.83
	PackNet-SfM [12]	Mv	Im	0.3434	7.328	11.60	0.3662	52.96	77.66	88.94
	Monodepth2 [11]	M*	Im	0.2442	4.518	9.781	0.3007	63.13	83.44	91.84
	baseline [ours]	Mv	Im	0.2547	4.614	9.586	0.3080	62.85	82.28	91.73
	R4Dyn-L [ours]	Mvr	Im	0.2187	3.950	8.719	0.2779	68.08	85.45	93.14
	R4Dyn-LI [ours]	Mvr	ImR	0.2055	3.706	8.316	0.2600	70.35	86.28	93.46
<i>Trucks</i>	Lin et al. [21]	GT	ImR	0.2356	3.248	8.410	0.2829	63.70	83.46	92.67
	Struct2Depth [4]	M*	Im	0.3711	7.153	12.26	0.4027	45.32	71.41	84.74
	PackNet-SfM [12]	Mv	Im	0.3472	6.561	11.48	0.3758	49.82	75.84	87.82
	Monodepth2 [11]	M*	Im	0.2659	5.330	10.42	0.3221	60.76	81.03	91.48
	baseline [ours]	Mv	Im	0.2751	4.782	10.25	0.3340	55.26	80.55	90.05
	R4Dyn-L [ours]	Mvr	Im	0.2457	4.184	9.739	0.3077	58.71	83.26	92.09
	R4Dyn-LI [ours]	Mvr	ImR	0.2369	4.219	9.493	0.2997	63.17	82.85	92.64
<i>Motorcycles</i>	Lin et al. [21]	GT	ImR	0.2529	3.473	8.292	0.2757	62.84	84.27	93.50
	Struct2Depth [4]	M*	Im	0.2328	3.110	8.026	0.2854	58.39	82.58	90.00
	PackNet-SfM [12]	Mv	Im	0.2007	2.575	7.062	0.2529	67.38	88.33	93.28
	Monodepth2 [11]	M*	Im	0.1900	2.457	6.693	0.2409	72.86	89.33	93.23
	baseline [ours]	Mv	Im	0.1849	2.481	6.856	0.2486	72.11	89.26	92.93
	R4Dyn-L [ours]	Mvr	Im	0.1833	2.534	6.885	0.2496	69.71	89.43	93.05
	R4Dyn-LI [ours]	Mvr	ImR	0.1730	2.401	6.519	0.2389	75.26	89.56	92.64

Table 7. Class(Cl.)-wise evaluation on the main individual *Vehicle* classes on the nuScenes [3] *day-clear* validation set. *NP* stands for *Non-Parked*. Table to be considered in conjunction with Table 8.

multi-path effects [23], resulting in an overestimated set of pixels around the horizon line, which is the image location where most radar detections lie on (as can be seen in Figure 8). As reported in Table 2, filtering the radar points (L3) led to a significant improvement in the estimations, which then improved further with our R4Dyn-L (L6), e.g. for the leading vehicle in the image.

For the input ablation (Figure 9), a single frame of radar input measurements (I2) did not improve the predictions, while the weak radar supervision and accumulating multi-

ple radar measurements (I4) eliminate the severe underestimation, but delivers artifacts on the shape of vehicles (e.g. oncoming van), which are improved by R4Dyn-LI (I6).

A.5.2 Class-wise Comparison with Related Works

Additionally to the absolute relative error (AbsRel) on object classes *Cars*, *Vehicles*, *Non-parked Vehicles* and *Pedestrians* reported in Table 1, we provide extensive class-wise results in Tables 7 and 8. Moreover, we plot a compari-

Cl.	Method	Sup.	Input	AbsRel	SqRel	RMSE	RMSE _{log}	δ_1	δ_2	δ_3
<i>Vehicles</i>	Lin et al. [21]	GT	ImR	0.2082	2.637	7.400	0.2668	73.08	88.99	95.08
	Struct2Depth [4]	M*	Im	0.3516	7.179	10.13	0.3612	54.53	79.25	89.63
	PackNet-SfM [12]	Mv	Im	0.2382	3.393	7.927	0.2885	67.48	87.71	94.14
	Monodepth2 [11]	M*	Im	0.2110	2.809	7.617	0.2726	68.89	87.85	94.50
	baseline [ours]	Mv	Im	0.2091	2.680	7.597	0.2775	67.91	87.33	93.91
	R4Dyn-L [ours]	Mvr	Im	0.1618	2.047	6.681	0.2273	77.16	92.72	96.76
	R4Dyn-LI [ours]	Mvr	ImR	0.1504	1.922	6.371	0.2188	80.51	92.77	96.75
<i>NP-Vehicles</i>	Lin et al. [21]	GT	ImR	0.2088	2.892	7.396	0.2597	74.98	89.46	94.96
	Struct2Depth [4]	M*	Im	0.3739	8.440	10.58	0.3643	53.17	77.87	88.58
	PackNet-SfM [12]	Mv	Im	0.2508	3.699	8.044	0.2923	66.24	86.47	93.39
	Monodepth2 [11]	M*	Im	0.2300	3.372	7.917	0.2815	66.25	86.16	93.29
	baseline [ours]	Mv	Im	0.2254	3.219	7.885	0.2880	66.67	84.78	92.27
	R4Dyn-L [ours]	Mvr	Im	0.1686	2.461	6.728	0.2268	77.86	91.87	95.97
	R4Dyn-LI [ours]	Mvr	ImR	0.1589	2.311	6.375	0.2162	80.86	92.61	96.16
<i>Pedestrians</i>	Lin et al. [21]	GT	ImR	0.2930	4.496	9.507	0.2966	59.51	84.11	93.09
	Struct2Depth [4]	M*	Im	0.2993	5.489	11.48	0.3714	49.37	74.98	87.35
	PackNet-SfM [12]	Mv	Im	0.2473	4.171	9.301	0.2987	61.93	86.17	92.33
	Monodepth2 [11]	M*	Im	0.2572	4.420	9.831	0.3087	61.46	86.04	91.88
	baseline [ours]	Mv	Im	0.2351	4.004	9.117	0.2961	66.20	86.37	92.08
	R4Dyn-L [ours]	Mvr	Im	0.2231	3.670	8.806	0.2853	66.90	87.00	92.42
	R4Dyn-LI [ours]	Mvr	ImR	0.2146	3.613	8.560	0.2763	70.74	86.73	92.41
<i>Objects</i>	Lin et al. [21]	GT	ImR	0.2227	2.767	7.319	0.2735	72.33	88.68	95.10
	Struct2Depth [4]	M*	Im	0.3400	6.552	9.726	0.3543	56.16	80.38	90.92
	PackNet-SfM [12]	Mv	Im	0.2383	3.405	7.757	0.2861	69.02	88.50	94.75
	Monodepth2 [11]	M*	Im	0.2123	2.832	7.592	0.2700	70.11	89.14	95.37
	baseline [ours]	Mv	Im	0.2032	2.548	7.278	0.2693	70.90	88.97	95.11
	R4Dyn-L [ours]	Mvr	Im	0.1631	1.997	6.522	0.2279	78.42	93.22	97.16
	R4Dyn-LI [ours]	Mvr	ImR	0.1551	2.020	6.367	0.2222	81.20	92.73	97.09
<i>Other</i>	Lin et al. [21]	GT	ImR	0.0781	0.693	4.268	0.1542	93.07	97.35	98.73
	Struct2Depth [4]	M*	Im	0.1873	3.254	6.823	0.2645	78.61	90.80	95.42
	PackNet-SfM [12]	Mv	Im	0.1141	1.723	5.777	0.2051	88.68	95.54	97.70
	Monodepth2 [11]	M*	Im	0.1117	1.344	5.354	0.1913	89.50	96.54	98.15
	baseline [ours]	Mv	Im	0.1010	1.207	5.223	0.1916	90.73	96.32	97.97
	R4Dyn-L [ours]	Mvr	Im	0.1036	1.194	5.290	0.1931	90.20	96.21	97.93
	R4Dyn-LI [ours]	Mvr	ImR	0.1003	1.197	5.190	0.1886	91.13	96.41	98.00

Table 8. Class(Cl.)-wise evaluation on *Vehicles* (includes all individual classes from Table 7, plus *Bicycles*, *Construction Vehicles* and *Emergency Vehicles*), *Non-Parked Vehicles*, *Pedestrians*, *Objects* (all object classes together) and *Other* (pixels that do not correspond to objects) on the nuScenes [3] *day-clear* validation set. Table to be considered in conjunction with Table 7.

son between Monodepth2 [11] and our R4Dyn in Figure 10 across the various classes. From the Figure, it can be seen that our approach outperformed Monodepth2 on every object class by a significant margin, which was especially large for the most dynamic ones, namely *Cars*, *Vehicles* and their *Non-Parked (NP)* variants. Considering Tables 7 and 8, the LiDAR-supervised work by Lin et al. [21], which uses radar as input, was able to deliver superior estimates on non-object classes, denoted as *Other* (e.g. *Driveable*

Surface and *Vegetation*). Nevertheless, our R4Dyn could obtain significantly lower errors and better scores on all object classes, except for *Trucks*, probably due to trucks being often static in urban areas (e.g. for loading and for deliveries), such as in the nuScenes dataset [3]. The results re-emphasize and confirm the effectiveness and the robustness of our approach across various safety critical dynamic objects, as well as the benefit of using radar sensors for depth estimation, especially as weak supervision.

A.5.3 Class-wise Comparison on Adverse Conditions

In Table 6 we provide class-wise results of ours and related methods under adverse weather settings. As for Table 5, which reports general errors in the same weather conditions, all approaches were trained on *day-clear* scenes (indicated as *clear* in the Table), therefore the values represent the ability of each method to generalize to rather different inputs. In particular, in Table 6 we provide AbsRel errors on safety critical traffic participants: *Cars*, *Vehicles* and *Pedestrians*. For these classes, our R4Dyn-LI was able to outperform related methods by a significant margin, under most settings. Again, we attribute this to the benefit of radar and the effectiveness of our techniques to incorporate it.

Method	Supervision	Input	AbsRel
Monodepth2 [11]	nuScenes: M*	Im	0.1162
R4Dyn [ours]	nuScenes: Mvr	Im Ψ	0.1028

Table 9. Transfer comparison to the KITTI validation set of models trained on nuScenes. Ψ indicates LiDAR sub-sampled like a radar.

A.5.4 Transfer Comparison: nuScenes \rightarrow KITTI

As written in Section 4.1, we used the nuScenes dataset [3] throughout our experiments, as it is to the best of our knowledge the only public dataset with data from a camera, an automotive radar, and a LiDAR to evaluate. On the other hand, the popular KITTI dataset [9] does not provide radar signals and has only limited dynamic scenes, which are the focus of our work. Nevertheless, radar sparsity and missing elevation can be simulated by sub-sampling a LiDAR signal, albeit leaving behind the highly complex radar noise modelling [23], as done also by Lin et al. [21]. Towards this end, we transferred our R4Dyn and Monodepth2 [11] models to the validation set of KITTI, without any fine-tuning, after training them on nuScenes [3]. We achieved this by cropping the KITTI images to the nuScenes format, and down-sampled the KITTI LiDAR to mimic the nuScenes radar: we kept only points within the radar field of view and sub-sampled them to reach the same low density (Section 3.2.1).

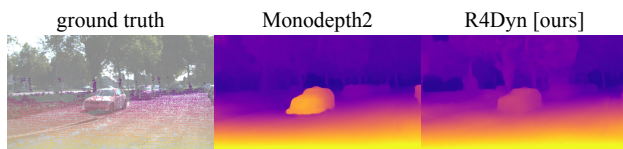


Figure 11. Qualitative example from a transfer from nuScenes to KITTI, without any fine-tuning of our R4Dyn, compared to Monodepth2 [11].

We provide the results of these experiments in Table 9, showing the generalization capability on significantly dif-

ferent data. Our R4Dyn outperforms Monodepth2 in this challenging transfer task. Qualitative results in Figure 11 confirm this and present similar outcomes to those seen in Figure 6, with Monodepth2 underestimating the depth of the oncoming vehicle. Despite the large domain gap and limited dynamic scenes (i.e. our focus), our 11.5% improvement on KITTI is substantial, again showing the effectiveness of our techniques to use radar in input and as weak supervision.

References

- [1] Jonathan T. Barron and Ben Poole. The fast bilateral solver. In *Proceedings of the European Conference on Computer Vision*, pages 617–632. Springer, 2016. 4
- [2] Shariq Farooq Bhat, Ibraheem Alhashim, and Peter Wonka. AdaBins: Depth estimation using adaptive bins. In *Proceedings of the IEEE/CVF Conference on Computer Vision and Pattern Recognition*, pages 4009–4018, 2021. 1
- [3] Holger Caesar, Varun Bankiti, Alex H Lang, Sourabh Vora, Venice Erin Liong, Qiang Xu, Anush Krishnan, Yu Pan, Giancarlo Baldan, and Oscar Beijbom. NuScenes: A multi-modal dataset for autonomous driving. In *Proceedings of the IEEE/CVF Conference on Computer Vision and Pattern Recognition*, pages 11621–11631, 2020. 1, 2, 3, 6, 7, 8, 9, 10, 11, 12, 13
- [4] Vincent Casser, Soeren Pirk, Reza Mahjourian, and Anelia Angelova. Depth prediction without the sensors: Leveraging structure for unsupervised learning from monocular videos. In *Proceedings of the AAAI Conference on Artificial Intelligence*, volume 33, pages 8001–8008, 2019. 2, 3, 5, 6, 7, 8, 10, 11, 12
- [5] Jia Deng, Wei Dong, Richard Socher, Li-Jia Li, Kai Li, and Li Fei-Fei. Imagenet: A large-scale hierarchical image database. In *Proceedings of the IEEE Conference on Computer Vision and Pattern Recognition*, pages 248–255, 2009. 6, 7
- [6] David Eigen, Christian Puhersch, and Rob Fergus. Depth map prediction from a single image using a multi-scale deep network. In *Advances in Neural Information Processing Systems*, pages 2366–2374, 2014. 2
- [7] Huan Fu, Mingming Gong, Chaohui Wang, Kayhan Batmanghelich, and Dacheng Tao. Deep ordinal regression network for monocular depth estimation. In *Proceedings of the IEEE/CVF Conference on Computer Vision and Pattern Recognition*, pages 2002–2011, 2018. 1, 2
- [8] Ravi Garg, Vijay Kumar B.G., Gustavo Carneiro, and Ian Reid. Unsupervised CNN for single view depth estimation: Geometry to the rescue. In *Proceedings of the European Conference of Computer Vision*, pages 740–756. Springer, 2016. 2
- [9] Andreas Geiger, Philip Lenz, Christoph Stiller, and Raquel Urtasun. Vision meets robotics: The KITTI dataset. *The International Journal of Robotics Research*, 32(11):1231–1237, Aug. 2013. 2, 3, 6, 7, 10, 13
- [10] Clement Godard, Oisín Mac Aodha, and Gabriel J. Brostow. Unsupervised monocular depth estimation with left-

- right consistency. In *Proceedings of the IEEE/CVF Conference on Computer Vision and Pattern Recognition*, pages 6602–6611, 2017. [2](#), [4](#), [9](#)
- [11] Clement Godard, Oisin Mac Aodha, Michael Firman, and Gabriel Brostow. Digging into self-supervised monocular depth estimation. In *Proceedings of the IEEE/CVF International Conference on Computer Vision*, pages 3827–3837, 2019. [1](#), [2](#), [3](#), [4](#), [5](#), [6](#), [7](#), [8](#), [9](#), [10](#), [11](#), [12](#), [13](#)
- [12] Vitor Guizilini, Rare Ambru, Sudeep Pillai, Allan Raventos, and Adrien Gaidon. 3D packing for self-supervised monocular depth estimation. In *Proceedings of the IEEE/CVF Conference on Computer Vision and Pattern Recognition*, pages 2482–2491, 2020. [2](#), [3](#), [4](#), [6](#), [7](#), [9](#), [10](#), [11](#), [12](#)
- [13] Vitor Guizilini, Rui Hou, Jie Li, Rares Ambrus, and Adrien Gaidon. Semantically-guided representation learning for self-supervised monocular depth. In *Proceedings of the International Conference on Learning Representations*, 2020. [2](#), [3](#)
- [14] Kaiming He, Xiangyu Zhang, Shaoqing Ren, and Jian Sun. Deep residual learning for image recognition. In *Proceedings of the IEEE/CVF Conference on Computer Vision and Pattern Recognition*, pages 770–778, 2016. [2](#), [6](#), [7](#)
- [15] Junhwa Hur and Stefan Roth. Self-supervised monocular scene flow estimation. In *Proceedings of the IEEE/CVF Conference on Computer Vision and Pattern Recognition*, pages 7394–7403, 2020. [3](#)
- [16] Jianbo Jiao, Ying Cao, Yibing Song, and Rynson W. H. Lau. Look deeper into depth: Monocular depth estimation with semantic booster and attention-driven loss. In *Proceedings of the European Conference on Computer Vision*, volume 11219, pages 55–71. Springer, 2018. [2](#)
- [17] Youngseok Kim, Jun Won Choi, and Dongsuk Kum. GRIF Net: Gated region of interest fusion network for robust 3D object detection from radar point cloud and monocular image. In *Proceedings of the IEEE/RSJ International Conference on Intelligent Robots and Systems*, pages 10857–10864, 2020. [2](#), [4](#), [9](#)
- [18] Diederik P. Kingma and Jimmy Ba. Adam: A method for stochastic optimization. In *Proceedings of the International Conference on Learning Representations*, 2015. [6](#)
- [19] Iro Laina, Christian Rupprecht, Vasileios Belagiannis, Federico Tombari, and Nassir Navab. Deeper depth prediction with fully convolutional residual networks. In *Proceedings of the IEEE International Conference on 3D Vision*, pages 239–248, 2016. [2](#)
- [20] Hanhan Li, Ariel Gordon, Hang Zhao, Vincent Casser, and Anelia Angelova. Unsupervised monocular depth learning in dynamic scenes. In *Proceedings of the Conference on Robot Learning*, 2020. [2](#), [3](#)
- [21] Juan-Ting Lin, Dengxin Dai, and Luc Van Gool. Depth estimation from monocular images and sparse radar data. In *Proceedings of the IEEE/RSJ International Conference on Intelligent Robots and Systems*, pages 10233–10240, 2020. [2](#), [5](#), [6](#), [7](#), [8](#), [10](#), [11](#), [12](#), [13](#)
- [22] Tsung-Yi Lin, Michael Maire, Serge Belongie, James Hays, Pietro Perona, Deva Ramanan, Piotr Dollár, and C. Lawrence Zitnick. Microsoft COCO: Common objects in context. In *Proceedings of the European Conference of Computer Vision*, pages 740–755. Springer, 2014. [8](#)
- [23] Yunfei Long, Daniel Morris, Xiaoming Liu, Marcos Castro, Punarjay Chakravarty, and Praveen Narayanan. Radar-camera pixel depth association for depth completion. In *Proceedings of the IEEE/CVF Conference on Computer Vision and Pattern Recognition*, 2021. [2](#), [3](#), [5](#), [11](#), [13](#)
- [24] Chenxu Luo, Zhenheng Yang, Peng Wang, Yang Wang, Wei Xu, Ram Nevatia, and Alan Yuille. Every pixel counts++: Joint learning of geometry and motion with 3D holistic understanding. *IEEE Transactions on Pattern Analysis and Machine Intelligence*, 42(10):2624–2641, Oct. 2020. [3](#)
- [25] Enrique D. Martí, Miguel Ángel de Miguel, Fernando García, and Joshué Pérez. A review of sensor technologies for perception in automated driving. *IEEE Intelligent Transportation Systems Magazine*, 11(4):94–108, 2019. [8](#)
- [26] Felix Nobis, Maximilian Geisslinger, Markus Weber, Johannes Betz, and Markus Lienkamp. A deep learning-based radar and camera sensor fusion architecture for object detection. In *Proceedings of the IEEE Sensor Data Fusion: Trends, Solutions, Applications*, pages 1–7, 2019. [2](#)
- [27] Adrian Lopez Rodriguez, Benjamin Busam, and Krystian Mikolajczyk. Project to Adapt: Domain adaptation for depth completion from noisy and sparse sensor data. In *Proceedings of the Asian Conference on Computer Vision*, volume 12622, pages 330–348. Springer, 2020. [3](#)
- [28] Nathan Silberman, Derek Hoiem, Pushmeet Kohli, and Rob Fergus. Indoor segmentation and support inference from RGBD images. In *Proceedings of the European Conference of Computer Vision*, pages 746–760. Springer, 2012. [2](#)
- [29] Carlo Tomasi and Roberto Manduchi. Bilateral filtering for gray and color images. In *Proceedings of the IEEE International Conference on Computer Vision*, pages 839–846, 1998. [4](#)
- [30] Shimon Ullman. The interpretation of structure from motion. *Proceedings of the Royal Society of London. Series B. Biological Sciences*, 203(1153):405–426, 1979 Jan 15. [1](#), [2](#)
- [31] Chien-Yao Wang, Alexey Bochkovskiy, and Hong-Yuan Mark Liao. Scaled-YOLOv4: Scaling cross stage partial network. In *Proceedings of the IEEE/CVF Conference on Computer Vision and Pattern Recognition*, pages 13029–13038, 2021. [6](#), [8](#)
- [32] Zhou Wang, Alan C Bovik, Hamid R Sheikh, and Eero P Simoncelli. Image quality assessment: from error visibility to structural similarity. *IEEE Transactions on Image Processing*, 13(4):600–612, April 2004. [4](#), [9](#)
- [33] Zhenheng Yang, Peng Wang, Yang Wang, Wei Xu, and Ram Nevatia. Every pixel counts: Unsupervised geometry learning with holistic 3D motion understanding. In *European Conference on Computer Vision Workshops*, pages 691–709. Springer, 2019. [3](#)
- [34] Tinghui Zhou, Matthew Brown, Noah Snavely, and David G. Lowe. Unsupervised learning of depth and ego-motion from video. In *Proceedings of the IEEE/CVF Conference on Computer Vision and Pattern Recognition*, pages 6612–6619, 2017. [2](#), [3](#), [4](#)